ELSEVIER

Journal of Nuclear Materials 270 (1999) 174–186

journal of nuclear materials

# Amorphization of $Zr_3Fe$ under electron irradiation

A.T. Motta [a,*], L.M. Howe [b], P.R. Okamoto [c]

[a] *Department of Nuclear Engineering, The Pennsylvania State University, 231 Sackett Bldg, University Park, PA 16802-1408, USA*
[b] *Atomic Energy of Canada, Ltd., Fuel Channels Division, Chalk River National Laboratories, Chalk River, Ontario, Canada K0J 1J0*
[c] *Materials Science Division, Argonne National Laboratory, Argonne IL 60439, USA*

Received 17 June 1998; accepted 20 October 1998

**Abstract**

The intermetallic compound $Zr_3Fe$ has been made amorphous by 0.9 MeV electron irradiation. By performing this irradiation in situ, it was possible to conduct a systematic study of the influence of temperature, dose rate, electron energy and specimen orientation on the amorphization process. The critical temperature and the critical dose for amorphization were determined, and shown to depend on dose rate. By varying the electron energy, we determined the displacement energies for the Zr and Fe atoms in $Zr_3Fe$, and showed that, at low electron energy, the amorphization rate is dependent on specimen orientation. We analyze these results in terms of a model based on amorphization occurring at a damage level where the modified free energy of the irradiated crystal exceeds the free energy of the amorphous phase. This model is shown to predict the amorphization kinetics, i.e. the critical temperature and critical dose for amorphization. We also compare amorphization induced by electron and ion irradiation. 

## 1. Introduction

The creation of amorphous phases from intermetallic compounds when submitted to electron irradiation has aroused great interest in the scientific community over the last decade [1–12]. This is because, in contrast with ion irradiation, amorphization under electron irradiation occurs in the absence of displacement cascades, and therefore, occurs by gradual accumulation of damage in the lattice in the form of point defects [13] or chemical disorder [14]. It was previously thought that the annealing mechanisms present in intermetallic compounds (lacking the annealing constraints present in ceramics and semiconductors) would overwhelm damage production and thus preclude amorphization by electron irradiation.

Research in the field evolved from survey studies where compounds were submitted to standard irradiation conditions (typically 1 MeV irradiation, below room temperature, at dose rates of $2 \times 10^{23}$–$3 \times 10^{23}$ e $m^{-2}$ $s^{-1}$) to determine which compounds were susceptible to amorphization [15,16], to more mechanistic studies which endeavor to find the conditions for amorphization from the kinetics of damage accumulation [17] and which investigate the nature of the transformation [4,18–20].

This study is part of a concerted effort to investigate amorphization phenomena by studying a given compound in depth, while submitting it to a range of irradiation conditions. In this way, we hope to glean a more complete picture of the amorphization process in this compound and thus derive conclusions that can be generalized to other compounds. This compound was chosen because previous studies have investigated its amorphization behavior under ion irradiation [21,22], its crystal structure is well known, and it fits well with our study of other compounds in the Zr–Fe–M system [17,23–25]. The results presented here for $Zr_3Fe$ show that the irradiation kinetics are paramount in determining amorphization behavior. The critical dose and the critical temperature behavior can be explained by simple arguments on how damage accumulates and anneals under irradiation. The significance of the results is also discussed in terms of current amorphization models and shown to support a model of amorphization by a

* Corresponding author. Fax: +1-814 865 8499; e-mail: atm2@psu.edu

0022-3115/99/$ – see front matter 
PII: S0022-3115(98)00657-6

lattice collapse induced by gradual accumulation of damage beyond a critical level, beyond which it becomes favorable to relax the long-range topological order so that short-range chemical order can be maintained.

## 2. Experimental methods

Samples of $Zr_3Fe$ were prepared at Chalk River Laboratories (CRL) by arc-melting the pure metals (Zr 99.95 at.% and Fe 99.9985 at.%) under an Ar atmosphere into an alloy with the overall composition $Zr_{0.8}Fe_{0.2}$. The samples were then heat-treated in a high vacuum (1.3 x $10^{-9}$ Pa or $10^{-11}$ Torr) furnace at 1073 K for 96 h, 1023 K for 72 h, and 1000 K for 48 h. This heat treatment produced the equilibrium mixture of orthorhombic $Zr_3Fe$ and hexagonal α-Zr, with minor amounts of tetragonal $Zr_2Fe$ still present. Thin disks suitable for electropolishing were prepared by slicing the arc-melted button using a diamond wafering blade, followed by mechanically polishing the slices to a thickness of 100–125 μm, and spark cutting. Electron-thin samples were prepared by electropolishing in a solution of 10% perchloric acid in methanol kept at 223 K.

Prior to irradiation, the samples were examined at CRL in a Philips CM-30 transmission electron microscope (TEM) at 295 keV with an energy-dispersive X-ray (EDX) attachment. These analyses confirmed the existence of the three phases – $Zr_3Fe$, α-Zr and trace amounts of $Zr_2Fe$. Each phase was positively identified by diffraction analysis in the TEM. In particular, the $Zr_3Fe$ phase was shown to be identical to that reported by Aubertin et al. [26], that is, an orthorhombic $BRe_3$-type structure with lattice parameters $a = 0.33$ nm, $b = 1.1$ nm, $c = 0.88$ nm. Compositional analysis of this phase by EDX yielded a composition close to Zr 75 at.%, Fe 25 at.%. Specific grains in the sample identified by EDX and diffraction prior to irradiation were later used for the irradiations, so that we were always sure to irradiate the correct phase.

Electron irradiations were conducted in the HVEM-Tandem Facility at Argonne National Laboratory, using 250–900 keV electrons, at temperatures ranging from 25 to 220 K. The temperature in the cold stage holder was known to within 1 K of the desired value. At the dose rates utilized, we estimate that the beam heating was less that 10 K. The vacuum in the microscope was better than $8 \times 10^{-5}$ Pa ($6 \times 10^{-7}$ Torr) during the irradiations.

The electron dose was monitored using two Faraday cups: the first placed just above the specimen captures the total electron current; the second placed at the level of the screen gives an estimate of the peak value of the electron flux profile, $J_0$. The electron flux is given by $J(r) = J_0 \exp[-(r/r_0)^2]$ where $J(r)$ is the electron flux (e $m^{-2}$ $s^{-1}$), $r$ is the distance from the center of the Gaussian, $J_0$ is the electron flux at $r = 0$ and $r_0$ is equal to $\sigma\sqrt{2}$ where $\sigma$ is the standard deviation of the Gaussian curve.

Individual grains identified as $Zr_3Fe$ during pre-irradiation TEM examination were irradiated with the electron beam until amorphous. Bright-field electron micrographs and diffraction patterns were taken at regular intervals. Amorphization was verified both by the disappearance of the bend contours in bright field and by the disappearance of the crystalline diffraction spots in diffraction mode. The bend contours were substituted by the standard milky appearance of amorphous zones, which are also insensitive to specimen tilting. The crystalline diffraction spot pattern was substituted by a halo characteristic of the amorphous phase. The corresponding distance of 0.25 nm calculated from the measured ring size in the negatives agrees well with the first nearest-neighbor distance of 0.26 nm determined for Zr–Fe glasses [27].

Since the smallest diffraction aperture in the HVEM comprises a region of 0.3 μm diameter, setting the dose-to-amorphization as the dose at which the diffraction spots disappear corresponds to stating that amorphization occurs at the dose necessary to create an amorphous zone of 0.3 μm in diameter. Series of irradiations were usually conducted within the same grain to avoid possible grain-to-grain variations. Considerable care was exercised to find and use markers that allowed for a constant repositioning of the beam, after defocusing to take pictures. In spite of these precautions, the random motion of the beam due to specimen drift and bending during irradiation, as well as minor errors in repositioning the beam and small variations in electron current contribute to somewhat 'blur' the contours of the beam, setting limits to the precision with which the dose can be determined.

After irradiation, the irradiated areas were examined at CRL for a detailed study of the amorphous zones and to use EDX to ascertain whether there were any compositional variations attendant on the transformation. The amorphous radius was measured from the negatives of the pictures taken during irradiation as a function of dose, for all the irradiation conditions examined.

## 3. Results

### 3.1. General remarks

There are a few observations that can be generalized to all the irradiation conditions we observed. Amorphization occurred in a spatially homogeneous manner throughout the whole area under the electron beam. No variation in chemical composition, or segregation of alloying elements was observed. We found that regardless of irradiation conditions, the amorphization

of $Zr_3Fe$ under electron irradiation follows a well-established sequence, as explained in the following.

The amorphization sequence observed in situ consisted of the following stages: (1) the samples start crystalline with a spot diffraction pattern (Fig. 1(a)); (2) at approximately 15% of the total irradiation time to amorphization, a faint ring starts to be visible in diffraction; at the same time, in bright field the background contrast becomes grayish and the higher order bend contours start to disappear (Fig. 1(b)); this trend continues throughout the irradiation until (3) at approximately 85% of the total irradiation time higher order reflections have disappeared, (usually only those spots that have a spacing similar to that of the amorphous ring remain). At that time, only the lower order bend contour remains, usually thinner and weakened (Fig. 1(c)). 4) Finally, at 100% of the amorphization time, all spots disappear and no bend contours are visible in imaging mode, be it bright field or dark field (Fig. 1(d)). This sequence occurs for short and for long irradiations and is common to other types of alloys we studied [25]. Although the criteria to judge the occurrence of stages are somewhat subjective, (e.g. when the amorphous ring is first visible) it was determined empirically that they were quite reproducible under the experimental conditions used. That is, we consistently found that the stages occurred at reproducible fractions of the total irradiation time.

The disappearance of most of the crystalline intensity occurs towards the end of the irradiation as seen before in other compounds [28]. Amorphization occurs, therefore, not as a nucleation and growth phenomenon (at least not on a scale of tenths of microns), but as a general collapse of the crystalline structure after a critical dose is delivered. It is possible that at the atomic level, there are heterophase fluctuations in the degree of order (or the degree of amorphization) but these are not individual amorphous/crystalline interfaces. The conclusion that amorphization is a second-order continuous transformation is also bolstered by molecular dynamics calculations performed by Devanathan and coworkers [11,29]. These calculations showed that at a time when diffuse rings are first visible in the diffraction pattern, on close examination it is virtually impossible to distinguish a well-defined interface separating amorphous and crystalline regions. In that sense, this is not a first-order transformation since there is no coexistence of amorphous and crystalline phase in regions where the critical dose has been delivered. Given the fact that systems under irradiation are open to an external energy and mass input, it is doubtful whether these classical thermodynamic descriptions of phase transitions as first or second order are useful or even applicable descriptions of irradiation phenomena [30].

### 3.2. Influence of irradiation temperature and dose rate on amorphization

The interface between the amorphous and the crystalline material at the edge of the beam is fairly sharp, as

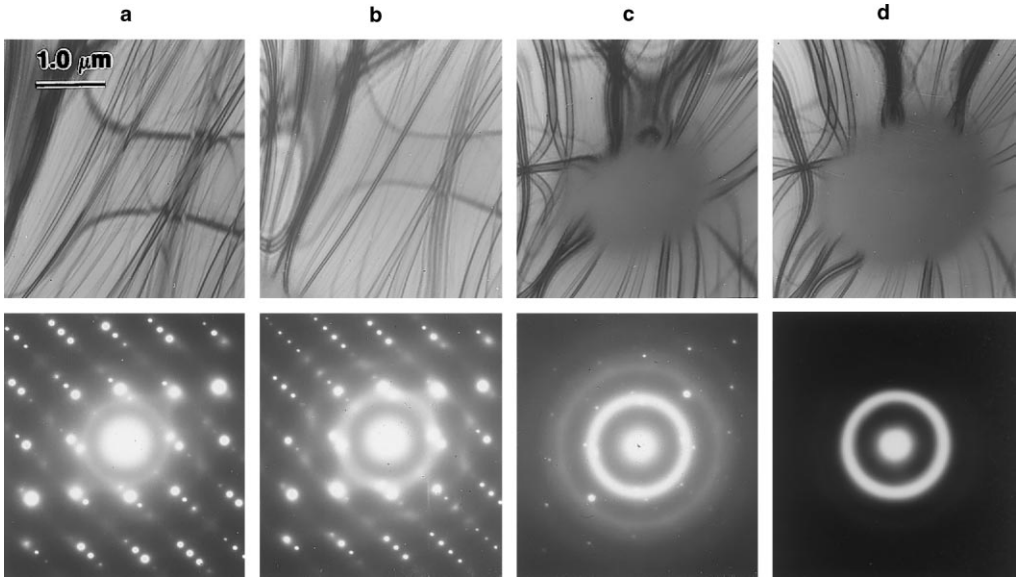


Fig. 1. Bright-field micrographs, and corresponding diffraction patterns of the stages of the in situ amorphization process of $Zr_3Fe$ by electron irradiation at 180 K for different times. (a) unirradiated specimen; (b) at 15% of the total time to amorphization, an amorphous ring is visible; (c) at 85% of the total time to amorphization, only the spots with spacing close to the amorphous ring remain; (d) completely amorphous sample, (with an amorphous spot bigger than the diffraction aperture), showing only an amorphous halo.

can be seen in Fig. 2(a) and (b). Thus, we can measure the amorphous radius as a function of dose with good precision. Fig. 3 shows the amorphous radius plotted against electron dose-to-amorphization for several irradiation temperatures. This graph was obtained by measuring the size of the amorphous spot from the negatives and using the fact that at the boundary of the crystalline and amorphous zones the dose received must, by definition, be the critical dose. The beam size shown in the figure corresponds to the beam inprint on the negative after a short exposure. We find that this choice is in good agreement with the final amorphous size in amorphization experiments performed at 17 K. Because the amorphous radius extends from the center to the edge of the beam, we are in fact irradiating the specimen within a range of dose rates. If an accurate dosimetry is performed, we can use this fact to study the influence of dose rate on amorphization.

Since several of the following results depend on an accurate evaluation of the electron flux, and measurement of the amorphous radii, it is useful to describe the data analysis in somewhat greater detail. As mentioned above, radial dependence of the beam intensity has been previously measured by Argonne National Laboratory as part of their beam characterization procedures and found to be gaussian in shape. Since the electron beam was oval rather than round, there were two major axes, for which the results have to agree. Thus, the amorphous radii in two perpendicular directions were used for the fitting. We used a short exposure bright-field image of the condensed electron beam to measure the size of the beam, $r_{\text{beam}}$, and the ratio between the two axes of the oval. This measured ratio can then be used in verifying the beam parameters.

We note that at any given time, the dose rate at the edge of the small and large axes of the amorphous oval has to be the same. Fig. 4 shows the electron flux (or the dose rates), at the final measured radii (when irradiation was stopped), as a function of temperature. The dose rates for the two axes agree very well, when the beam sizes from the negative are used.

Performing a horizontal cut on Fig. 3 (thus, at constant dose rate) and plotting the intercept of each curve against temperature, the classical exponential dependence of dose-to-amorphization on irradiation temperature is obtained [3]. The critical dose-to-amorphization is dependent on enough accumulation of defects to destabilize the crystalline solid with respect to the amorphous structure.

By performing several cuts, and using the electron flux determined by the two independent Faraday cup measurements, it was possible to obtain the dependence of the dose-to-amorphization on the dose rate. For different radii, the dose rate varies following the Gaussian shape of the beam. Then if the dose-to-amorphization were the same for all dose rates, a vertical line would be obtained, indicating that the dose-to-amorphization at $r = 0$ is the same as that at $r = r_{\text{beam}}$. As shown in Fig. 3, this is indeed the case for the experiments conducted at low temperature (28 K): the amorphous spot spreads from the center and eventually reaches the size of the electron beam, with the transformation occurring at a constant dose. As the temperature is increased to 100 K, there is a slight deviation

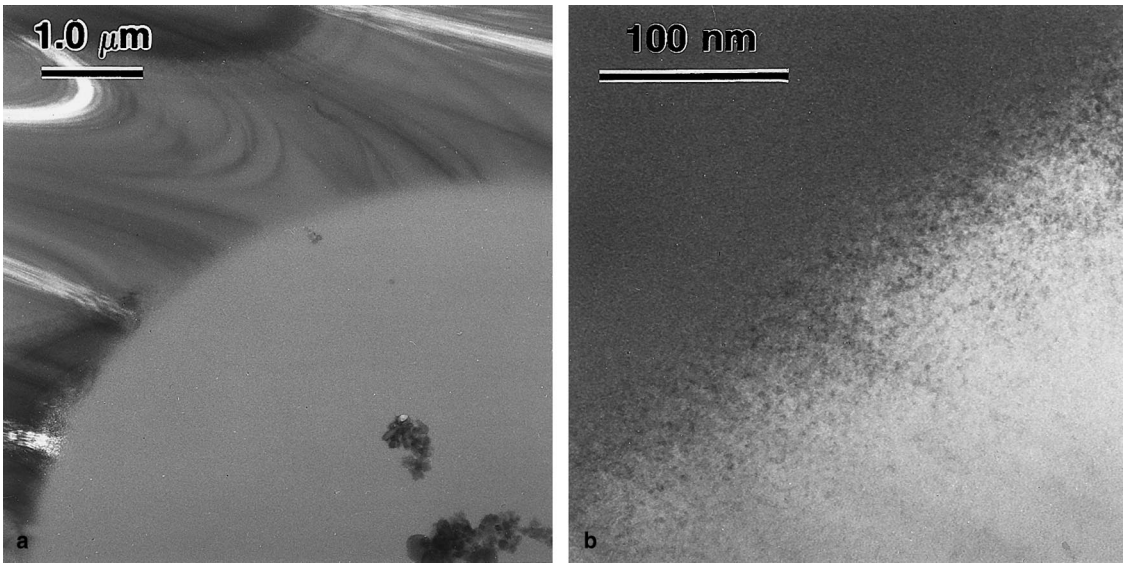


Fig. 2. (a) Low magnification dark-field micrograph and (b) high magnification bright-field micrograph of the amorphous/crystalline interface. The interface is sharp enough that there is little error in measuring the size of the amorphous spot.

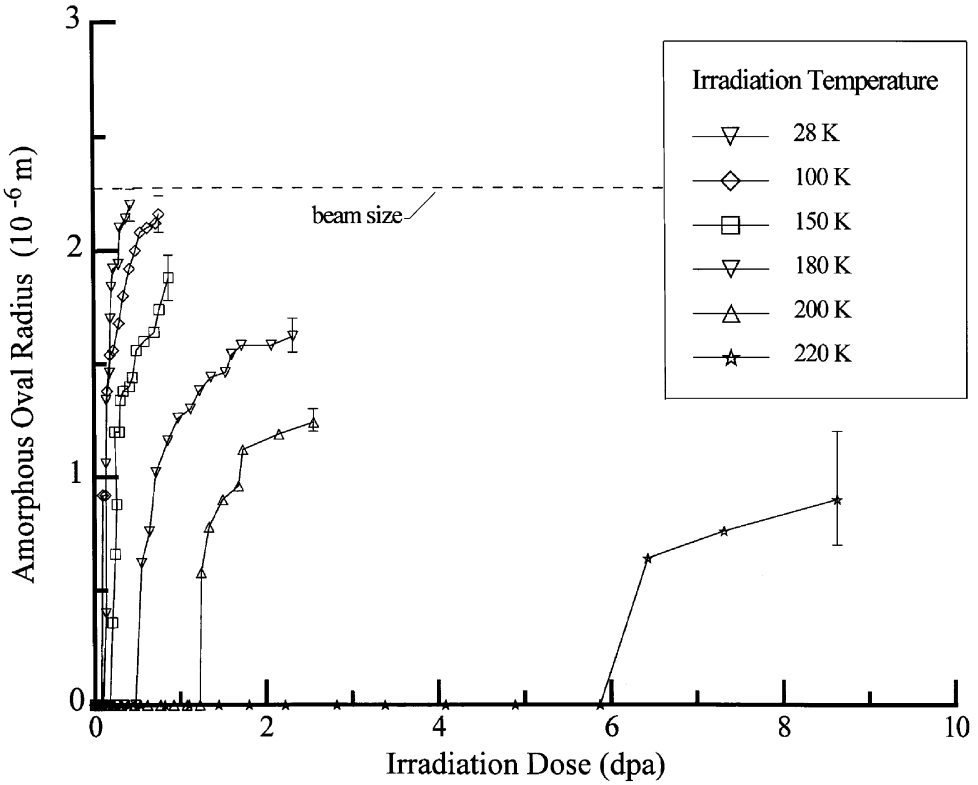


Fig. 3. Amorphous radius versus dose for several irradiation temperatures during amorphization of $Zr_3Fe$ by electron irradiation.

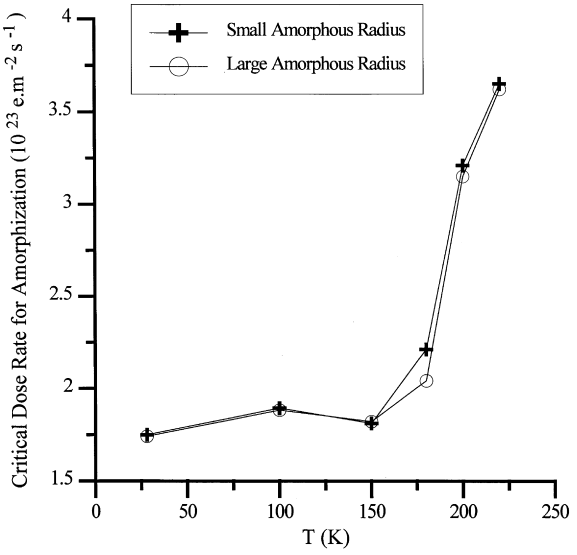


Fig. 4. Critical dose rate for amorphization under electron irradiation calculated from the final values of the two axes of the amorphous oval.

from this behavior at $r/r_{beam} = 0.9$. The final size of the amorphous spot, however, is still equal to the beam size. As the temperature is further increased to 180 K, the deviation from the dose rate-independent behavior occurs at $r/r_{beam} = 0.3 - 0.4$ and now the final amorphous zone size is smaller than the beam size: the final amorphous spot size is equal to $0.75 \times r_{beam}$. These trends continue as the temperature is further increased to 220 K: at that temperature the final size of the amorphous zone is only $0.35 \times r_{beam}$.

Since the irradiations were stopped at a time when the amorphous radius expansion had slowed down appreciably, the fluxes in Fig. 4 are close to the critical dose rate for amorphization, below which no amorphization is possible at a given temperature. A better estimate of this critical dose rate can be achieved by calculating the dose rate at the saturation amorphous radius. Fig. 5 shows the critical dose rate versus temperature determined by this method. For dose rates less than the critical dose rate, the annealing rate is higher than the damage rate and no damage can accumulate. The upper and lower dose rate limits available in the beam we used are also shown. The critical dose rate increases with temperature, until at 220 K the critical dose rate is also the highest dose rate available within

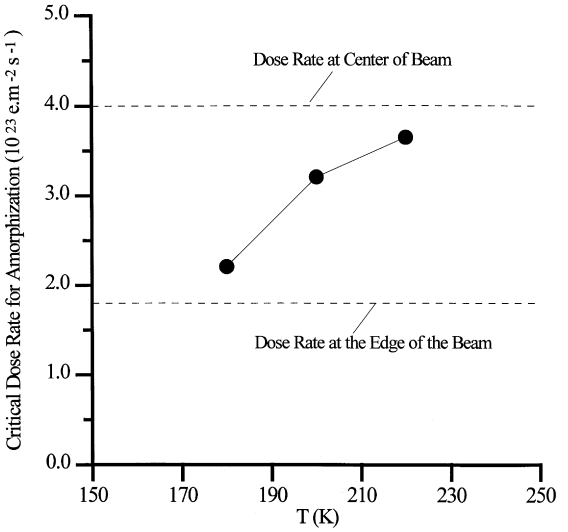


Fig. 5. Critical dose rate for amorphization from the extrapolated saturation values of the amorphous oval as a function of temperature.

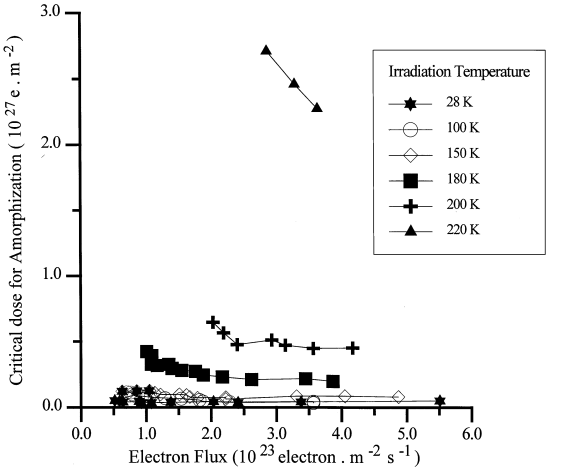


Fig. 6. Dose to amorphization versus electron flux for several irradiation temperatures.

the beam. This means that conceivably for a higher intensity beam, amorphization would be achievable at temperatures above 220 K. Thus the critical temperature for amorphization under electron irradiation is dependent on the dose rate. However, since the annealing rate increases exponentially with temperature, the dose rate would also have to increase exponentially to still allow amorphization. For the dose rates achievable in practical irradiation conditions, the change in critical temperature due to increased dose rate is of the order of tens of degrees K.

Fig. 6 shows the dose-to-amorphization as a function of dose rate for various temperatures. The dose-to-amorphization decreases as the dose rate increases. This effect becomes more pronounced as the temperature is increased to 180–220 K.

### 3.3. Influence of electron energy

The influence of electron energy was investigated by irradiating the material at electron energies ranging from 200 to 900 at 25 K. [23]. At this low temperature the defect mobility is assumed to be low enough that we can neglect thermal annealing. Fig. 7 shows the dose-to-amorphization as a function of electron energy at 25 K; the actual dose-to-amorphization could be up to 10% lower than the dose measured here, because of the discrete time steps taken during irradiation. In the region between 900 and 700 keV as the electron energy decreases, the dose-to-amorphization remains constant. Between 700 and 600 keV there is a sudden increase in the dose-to-amorphization, which then remains constant between 600 and 450 keV. Below 400 keV, the dose-to-amorphization increases quickly, and amorphization is not achieved below 250 keV. At 250 keV, amorphization was achieved only with great difficulty. Similar type of behavior was observed for other compounds such as $ZrCr_2$ [31] and $Zr_2Fe$ [32]. By fitting the measured dose-to-amorphization with the method described in Section 4.4 we estimated the displacement energies for the Fe and Zr atoms in the $Zr_3Fe$ compound. The values are $E_d^{Zr} = 26$ eV and $E_d^{Fe} = 18$ eV [32].

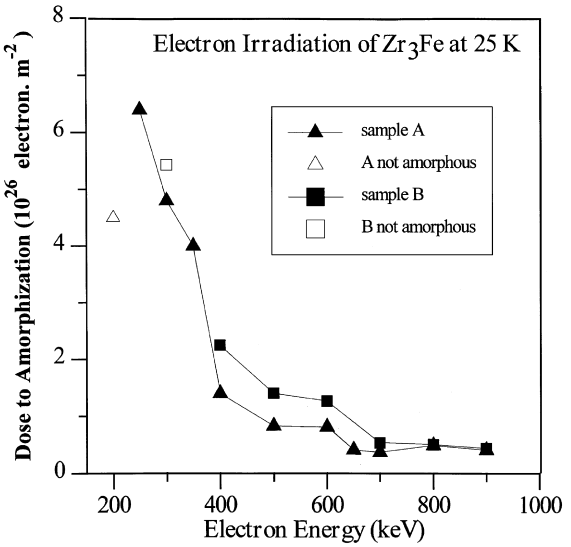


Fig. 7. Electron dose to amorphization versus electron energy for amorphization of $Zr_3Fe$ performed at 25 K. The different curves are for two different samples, having different impurity concentrations.

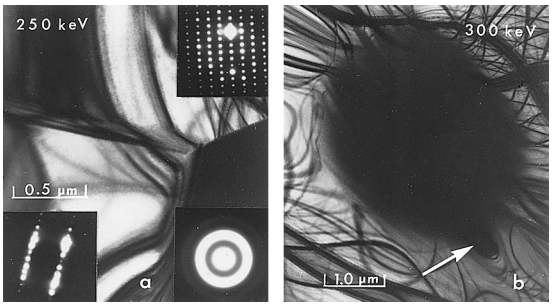


Fig. 8. (a) Triple point junction in $Zr_3Fe$ showing preferential amorphization in one of the grains during electron irradiation at 250 keV, at 28 K (the beam was located at the triple junction and the three grains irradiated simultaneously); (b) amorphous spot formed during electron irradiation at 300 keV, showing amorphous wisps along bend contours.

### 3.4. Influence of specimen orientation relative to electron beam

Because the displacement energy varies with crystallographic orientation, when the electron energy is low enough, the electrons can displace the atoms along certain crystallographic orientations, but not along others. Fig. 8 shows the irradiation of a triple point at 250 keV performed such that three $Zr_3Fe$ grains were irradiated at the same time. The experiment showed that only one of the three grains underwent amorphization during irradiation [22] as shown in Fig. 8. We interpret this result as evidence of an orientation dependence of the displacement energy, and consequently of amorphization. An orientation dependence of amorphization in $Zr_3Al$ has also been observed by Mori et al. [33].

In this work, we observed evidence of an orientation dependence of amorphization for irradiations at energies up to 350 keV. Fig. 8 also shows the amorphous spot from an irradiation conducted at 300 keV. Along the bend contours amorphization was easier, as can be seen from the amorphous 'wisps', arrowed in the picture. In these regions, the amorphous zone extends beyond the central oval, along bend contours. This is seen in more detail in Fig. 9. The likely reason for this is that at 250–350 keV, the transferred energy can exceed the displacement energy along certain directions, but not along others. Above 400 keV, lattice displacements can occur in any crystallographic direction.

## 4. Discussion

### 4.1. General remarks

Amorphization is the loss of long-range topological order, as evidenced by the disappearance of crystalline spots in the electron diffraction pattern, and the appearance of an amorphous halo. Such a transformation involves an increase in free energy relative to that of the unirradiated solid. This increase in free energy is brought about by the damage caused by the interaction of the energetic particles (in this case electrons) which impart energy to the atoms in the solid and displaces them from their lattice positions or from their preferred sites. Damage accumulates in the material in the form of isolated point defects and anti-site defects. As the free energy of the irradiated solid increases and surpasses that of the amorphous alloy of the equivalent composition, a driving force is created for the transformation of the damaged crystalline compound into an amorphous compound.

Alternatively, one could describe the amorphization condition in terms of the modified Lindemann criterion

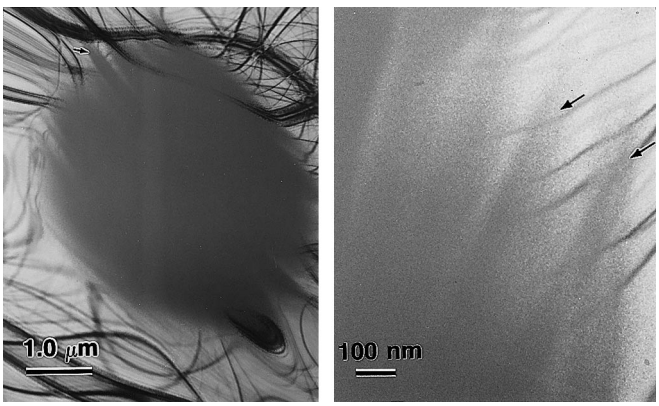


Fig. 9. Bright-field micrograph showing amorphous wisps formed during irradiation of $Zr_3Fe$ at 300 keV. The wisps follow bend contours that were present during irradiation showing further evidence that the displacement energy depends on the crystalline orientation.

[11], which states that amorphization occurs whenever a critical mean-square static displacement $\langle x^2 \rangle$ is achieved in the crystal, as a result of all defect accumulation processes. Molecular dynamics computer simulations show that amorphization always occurs at a fixed value of $\langle x^2 \rangle$ whether the origin of the increase in mean square displacements is point defects, antisite defects or thermal motion [7].

From a thermodynamic point of view there is no difference between the two criteria. Both approaches to describe amorphization assume that amorphization occurs when the amount of disorder of the defected crystal becomes equal to that of the amorphous phase. The only significant difference is that the two approaches use different disorder parameters to characterize the thermodynamics of the transformation. The free energy approach used in the present paper explicitly focuses on the contributions of the radiation-produced changes in chemical disorder and the non-equilibrium vacancy ($C_v$) and interstitial ($C_i$) concentrations to the excess free energy, $\Delta G_{irr}$, in driving amorphization. Hence, the free energy approach uses the Bragg–Williams LRO parameter, **S**, $C_v$ and $C_i$ to characterize its disorder parameter, $\Delta G_{irr}$.

The Lindemann criterion also uses a single disorder parameter, the magnitude of the mean square static displacement, as a generic measure of the total disorder of the material, and assumes that thermodynamic melting in the solid state (i.e. amorphization) occurs when the sum of the static and dynamic mean square displacement reaches a critical value equal to that for melting of the defect free crystal. As shown in Refs. [7,11], this generalized version of the Lindemann hypothesis can be formally expressed in the form of a scaling relationship for the reduced quantities $T_m^d$ $T_m^0$, $\theta_d^2$, $\theta_0^2$, and $\tau_d$, $\tau_0$, i.e.

$$\frac{T_m^d}{T_m^0} = \frac{\theta_d^2}{\theta_0^2} = \frac{\tau_d}{\tau_0} = \left[1 - \frac{\langle \mu_{sta}^2 \rangle}{\langle \mu_{cri}^2 \rangle}\right], \tag{1}$$

where $T_m^d$, $\theta_d$ and $\tau_d$ are, respectively, the thermodynamic melting temperature, the Debye temperature and average shear modulus of the defected crystal, and $T_m^o$, $\theta_0$ and $\tau_0$ are the corresponding values for the defect-free crystal.

It is possible in principle to relate the point defects and chemical disorder created by irradiation to a mean square displacement. If this were done it would be possible to compare the damage caused by irradiation to a critical mean square displacement and thus predict amorphization using the modified Lindeman criterion. However no simple general expressions exist to relate the defect concentration to a mean square displacement, so we use the free energy description of amorphization in this work.

### 4.2. Model for amorphization in intermetallic compounds

Once the driving force for the transformation exists, kinetics determine when amorphization occurs. Because amorphization is easier at low temperature, it does not depend on long range diffusion and atomic rearrangements and is likely effected by local rotations and small displacements within the unit cell. Also, since electron irradiation creates damage homogeneously throughout the material, the transformation takes place simultaneously all over the material. Since only local atomic rearrangements are involved, the transformation can take place immediately once the driving force has developed. The electron dose necessary for amorphization (the dose-to-amorphization) is then determined by the kinetics of damage accumulation and simultaneous annealing. The condition for amorphization can be written as

$$\Delta G_{irr} \geqslant \Delta G_{ca}, \tag{2}$$

where $\Delta G_{ca}$ is the difference in free energy between the crystalline and amorphous phases

$$\Delta G_{ca} = G_a - G_c \tag{3}$$

and where $\Delta G_{irr}$is the increase in free energy from irradiation due to all the possible mechanisms of energy storage in the solid such as the creation of point defects, increase in chemical disorder, presence of dislocations, stacking faults, etc:

$$\Delta G_{irr} = \Delta G_{def} + \Delta G_{dis} = G_{irr} - G_{unirr} = \sum_i \Delta G_{irr}^i. \tag{4}$$

Both $\Delta G_{def}$ and $\Delta G_{dis}$ are a function of the concentration of point defects and of anti-site defects under irradiation. These can be evaluated using rate theory [34]. Assuming that the different processes of defect accumulation are independent of each other and making approximations such as using the Bragg–Williams description of long-range-order (LRO) to calculate the free energy change to disorder, it is possible to evaluate $\Delta G_{irr}$ and compare it to $\Delta G_{ca}$ [13]. The change in free energy with irradiation is written as

$$\begin{aligned}\Delta G_{irr} &= \Delta G_{def} + \Delta G_{dis} \\ &= \sum_j \left[C_j E_j - T\Delta S_i\right] + \Delta C_{pab} N\Omega - T\Delta S_{dis}\end{aligned} \tag{5}$$

where $\Delta G_{def}$ is the increase in free energy due to the accumulation of point defects and $\Delta G_{dis}$ is the increase in free energy due to increase in chemical disorder, $C_j$ is the concentration of defect $j$, $E_j$ its formation energy, $\Omega$ is the ordering energy, $\Delta S_j$ the configurational entropy change from introducing point defects and $\Delta S_{dis}$ is the configurational entropy change due to the introduction of anti-site defects [35]. The change in the number of A–B pairs per mol as a result of changes in the Bragg–Williams long-range order parameter, **S**, for $Zr_3Fe$ is,

$$\Delta C_{\mathrm{pab}} = N\,[A(1-\mathbf{S}^2) + B(1-\mathbf{S})], \tag{6}$$

where $N$ is the number of lattice sites per mol. For $Zr_3Fe$ the constants $A$ and $B$ are 3/4 and 1/4, respectively. It is important to note that the configurational entropy as calculated here is only defined in the crystalline phase. The concentration of defects and the order parameter can be calculated using chemical rate theory as explained in Ref. [28] and the several order–disorder kinetics expressions available [36,37].

The concentration of defects is given by the rate equations:

$$\frac{\partial C_{\mathrm{v}}}{\partial t} = k - K_{\mathrm{iv}} C_{\mathrm{i}} C_{\mathrm{v}} - \sum_j S_{j\mathrm{v}} D_{\mathrm{v}}\, C_{\mathrm{v}}, \tag{7}$$

$$\frac{\partial C_{\mathrm{i}}}{\partial t} = k - K_{\mathrm{iv}} C_{\mathrm{i}} C_{\mathrm{v}} - \sum_j S_{j\mathrm{i}} D_{\mathrm{i}}\, C_{\mathrm{i}}, \tag{8}$$

where $C_{\mathrm{v}}$ and $C_{\mathrm{i}}$ are the concentrations of vacancies and interstitials, $k$ is the dose rate (dpa $\mathrm{s}^{-1}$), $K_{\mathrm{iv}}$ is the recombination coefficient, $D_{\mathrm{i}}$ and $D_{\mathrm{v}}$ are the diffusion coefficients of interstitials and vacancies, and the $S_{j\mathrm{v}}$ and $S_{j\mathrm{i}}$ are the sink strengths for vacancies and interstitials for all the individual sinks present in the material, including the foil surface. Calculations have shown that for electron irradiation of thin-foils the foil surface is usually the dominant defect sink [24].

These equations have been used to predict irradiation phenomena in alloys, and have been applied to the amorphization problem [13,34,38]. For example, under irradiation conditions used during electron irradiation in a TEM, steady state is not reached, and a recombination-dominated regime exists for the whole irradiation time [28]. When one type of defect is much faster than the other, the foil surfaces dominate defect annihilation creating a supersaturation of the slow defect in the material [13], which makes amorphization possible.

We should note that although Eq. (7) and Eq. (8) have been used to predict defect accumulation in intermetallic compounds in the examples above, this has been done only in an approximate manner. The rigorous application of rate theory to ordered intermetallic compounds (which has not yet been achieved) would involve writing separate equations for the many different defects (vacancies and interstitials in either sublattice, and anti-site defects). This introduces many new parameters (defect migration and formation energies, recombination reaction volumes, etc.) which have to be supplied for the system of equations to be solved. Further, new terms would appear in these equations for the reactions among these defects. The solutions below can be considered to be a simplified case in which only two defect (a fast and a slow defect) are present, and migration is spatially isotropic. In particular the normal relationship of migration energies found in metals (i.e. interstitials are fast diffusers and vacancies slow) can be reversed in intermetallic compounds [39]. If however, one of the defects is much faster than the other at the irradiation temperature (by a factor greater than $10^5$), then the solution shown in Eqs. (9) and (10) is valid.

Using this approach, and with the above caveats, it is possible to model the whole dose-to-amorphization versus temperature curve, as well as the kinetics of amorphization. Both the critical temperature and the critical dose are derived naturally from the model. One problem with this approach is that although the amorphization process is clearly cooperative, no interaction between defects is explicitly assumed.

### 4.3. Application of the model to $Zr_3Fe$

When the model above is applied to amorphization under electron irradiation at low temperature, under normal irradiation conditions, and when one defect is much faster than the other, we find that during the time required to render the sample amorphous, the point defect accumulation and annihilation do not reach a steady state. We also find that electron irradiations leading to amorphization are usually performed in the low temperature recombination-dominated regime. Assuming that interstitials are the fast defect and vacancy the slow defect (the conclusions would not change if the mobilities were reversed), then within the approach to steady state (within the recombination dominated regime), the concentration of defects is given by

$$C_{\mathrm{v}} = A_1 \left(\frac{k}{K_{\mathrm{iv}}}\right)^{1/4} \sqrt{kt}, \tag{9}$$

$$C_{\mathrm{i}} = A_2 \left(\frac{k}{K_{\mathrm{iv}}}\right)^{1/4} \frac{1}{\sqrt{kt}}, \tag{10}$$

where $A_1$ and $A_2$ are constants. The dose rate $k$ is given by

$$k = x_{\mathrm{Fe}} k_{\mathrm{Fe}} + x_{\mathrm{Zr}} k_{\mathrm{Zr}} = \Phi_{\mathrm{e}} [x_{\mathrm{Fe}} \sigma_{\mathrm{d}}^{\mathrm{Fe}}(E, E_{\mathrm{d}}^{\mathrm{Fe}}) + x_{\mathrm{Zr}} \sigma_{\mathrm{d}}^{\mathrm{Zr}}(E, E_{\mathrm{d}}^{\mathrm{Zr}})], \tag{11}$$

where $\Phi_{\mathrm{e}}$ is the electron flux (e $\mathrm{m}^{-2}$ $\mathrm{s}^{-1}$), $x_{\mathrm{Fe}}$ and $x_{\mathrm{Zr}}$ are the atomic fractions of Zr and Fe in the compound, and the $E_{\mathrm{d}}$'s are the displacement energies of the individual atoms in the compound. The displacement cross sections can be obtained from Oen's tables for an electron energy of 900 keV, and for the displacement energies measured in Section 3 as $\sigma_{\mathrm{d}}^{\mathrm{Fe}} = 60.4$ barns and $\sigma_{\mathrm{d}}^{\mathrm{Zr}} = 20.1$ barns. Thus

$$k\ (\mathrm{dpa/s}) = 45.3 \times 10^{-20} \Phi_{\mathrm{e}}, \tag{12}$$

where the flux is given in electron $\mathrm{m}^{-2}$ $\mathrm{s}^{-1}$.

Because of the difference in mobility of the defects one defect can reach the surface, and the other defect accumulates in the lattice. Thus, according to Eqs. (9) and (10) for a given electron dose, at a higher dose rate

we should expect a slightly higher defect concentration and thus a lower critical dose for amorphization. In the high temperature region, near the critical temperature for amorphization, we can use the following equation, which relates the dose-to-amorphization ($dpa_{final}$) to the dose rate and the mobility of the fast defect [13]

$$dpa_{final} k^{1/2} = B e^{(-E_m^i/2K_B T)}, \quad (13)$$

where $E_m^i$ is the interstitial migration energy, $K_B$ is Boltzmann's constant, and $B$ is a constant. Using the model above, we can plot $dpa_{final}.k^{1/2}$ against inverse temperature in an Arrhenius plot, as shown in Fig. 10. The lines are just included to guide the eye. We note that there is an athermal regime below 150 K and an activated regime above 200 K, for which the activation energy is 0.12 eV. This means that according to the model expressed in Eq. (13), the migration energy of the fast defect is 0.24 eV. Using Eq. (13), we can find the ratio $T_c^{high}/T_c^{low}$, where $T_c^{high}$ and $T_c^{low}$ are the critical temperatures for high dose rate ($k_{high}$) and low dose rate ($k_{low}$) irradiation. Manipulating Eq. (13), we obtain

$$\frac{E_m^i}{2K_B}\left(\frac{-1}{T_c^{low}} + \frac{1}{T_c^{high}}\right) = \ln\left[\left(\frac{k_{low}}{k_{high}}\right)^{1/2}\right]. \quad (14)$$

For $E_m^i = 0.24$ eV [13], $k_{low} = 1.1 \times 10^{-3}$ dpa $s^{-1}$ and $k_{high} = 1.6 \times 10^{-3}$ dpa $s^{-1}$, we find that $T_c$ changes by about 10 K, in good agreement with observations.

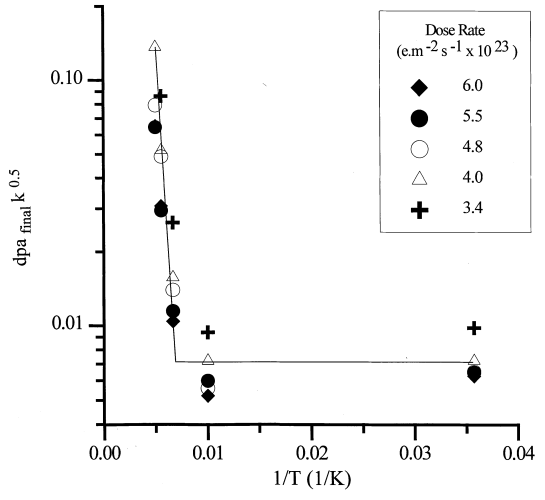


Fig. 10. Dose to amorphization times the square root of dose rate versus inverse temperature. The lines are fits to data and indicate that there are two regimes, an athermal regime at low temperature and a thermally activated regime at higher temperature, with an activation energy of 0.12 eV.

### 4.4. Analysis of energy dependence of amorphization

The results of the energy dependence experiments shown in Section 3.3 can be analyzed in terms of a composite displacement cross section dominated at high energies by displacements of Zr and Fe, by displacements of Fe at intermediate energies (400–600 keV) and by secondary displacements of lattice atoms by recoil impurity atoms (principally O) at low energies (below 400 keV), similarly to the observations of displacements by subthreshold irradiations [40–43].

As mentioned above, amorphization occurs when the dose received is equal to the critical dose for amorphization, i.e., at a constant dose in dpa, which is specific for each intermetallic compound. Consequently for each electron energy $E$ at amorphization

$$D(E) = (\phi t)_{am}(E)\sigma_d(E) = (\phi t)_{am}(E)\sum_i x_i \sigma_d^i(E_d^i, E) = D_{crit}, \quad (15)$$

where $D_{crit}$ is the dose-to-amorphization, $(\phi t)_{am}$ is the electron fluence at amorphization, $x_i$ is the concentration of element i in the compound, $\sigma_d^i(E_d^i, E)$ is the displacement cross section, $E_d^i$ is the displacement threshold energy. Eq. (15) states that when we multiply the values of the dose-to-amorphization as a function of energy (as given for example in Fig. 7), by the weighted displacement cross section (obtained by the tabulations of Oen [44], the result should be independent of energy. Since the values from Oen's tables are dependent upon the displacement energy, it is possible to find the set of displacement energies that best fits the experimental data. For more detailed information, see Ref. [23,31,32].

As mentioned above, the specific values of the displacement energies obtained for $Zr_3Fe$ which has an orthorhombic structure were $E_d^{Zr} = 26$ eV and $E_d^{Fe} = 18$ eV [32]. By comparison, values obtained for $ZrCr_2$ [31] and $Zr_2Fe$ [32] using the same analysis procedure were as follows:

(i) $ZrCr_2$ (a cubic Laves phase): $E_d^{Zr} = 22$ eV and $E_d^{Fe} = 23$ eV.

(ii) $Zr_2Fe$ (body centered tetragonal) $E_d^{Zr} = 25$ eV and $E_d^{Fe} = 27$ eV.

Taking the displacements produced by a secondary displacement mechanism into account, yields values for $E_d^O$ of 12, 8 and 4 eV for $Zr_3Fe$, $Zr_2Fe$ and $ZrCr_2$, respectively [31,32]. The method used above for determining the displacement threshold energies for the constituent atoms in $Zr_3Fe$, $ZrCr_2$, and $ZrFe_2$ is generally applicable to any intermetallic compound that undergoes a transition from the crystalline to amorphous state during low temperature electron irradiation. It is, therefore, complementary to other experimental methods employed for determining threshold displacement energies in intermetallic compounds, such as the mea-

surement of irradiation induced changes in electrical resistivity [45,46] and in the critical temperature for transition from the superconducting to the normal state in A15 compounds like $Nb_3Ge$ or $V_3Si$ [46]. Molecular-dynamics calculations have also been used for determining threshold displacment energies along specific directions in intermetallic compounds such as $Ni_3Al$ [47] and CuTi [48].

### 4.5. Comparison with ion irradiation

Fig. 11 shows the temperature dependence of the dose-to-amorphization of $Zr_3Fe$ for ion and electron irradiation. It is clear from the figure that amorphization by ion irradiation occurs in a considerably wider range of temperatures than amorphization by electron irradiation. For ion irradiation the critical temperature for amorphization of $Zr_3Fe$ is approximately 580 K [22]. This difference can be qualitatively understood in terms of the model described in Sections 4.2 and 4.3. Under ion irradiation large amounts of energy can be transferred by the incident ion to the atoms in the target. These energetic atoms in turn transfer their energy to other atoms in a localized region nearby the original impact, causing a displacement cascade. In these cascades, the effective displacement rate is very high, and the annealing mechanisms do not have time to recrystallize the material before the cascade region cools down and creates an amorphous region. A variation of this model is to have multiple cascade hits necessary to form an amorphous zone. In particular, cascades of different densities are produced by ions of different masses and energies [22], which is the likely reason why the critical temperature for amorphization under ion irradiation is a function of the ion type [19].

It is also interesting to note that the dose-to-amorphization for $Zr_3Fe$ under ion irradiation increases by more than a factor of four at the critical temperature for amorphization of $Zr_3Fe$ by electron irradiation. This agrees with the hypothesis that an annealing stage is activated at that temperature which makes ion-irradiation-induced amorphization difficult, but not impossible.

Once the amorphous region is formed, the activation energy for recrystallization is higher than that for an-

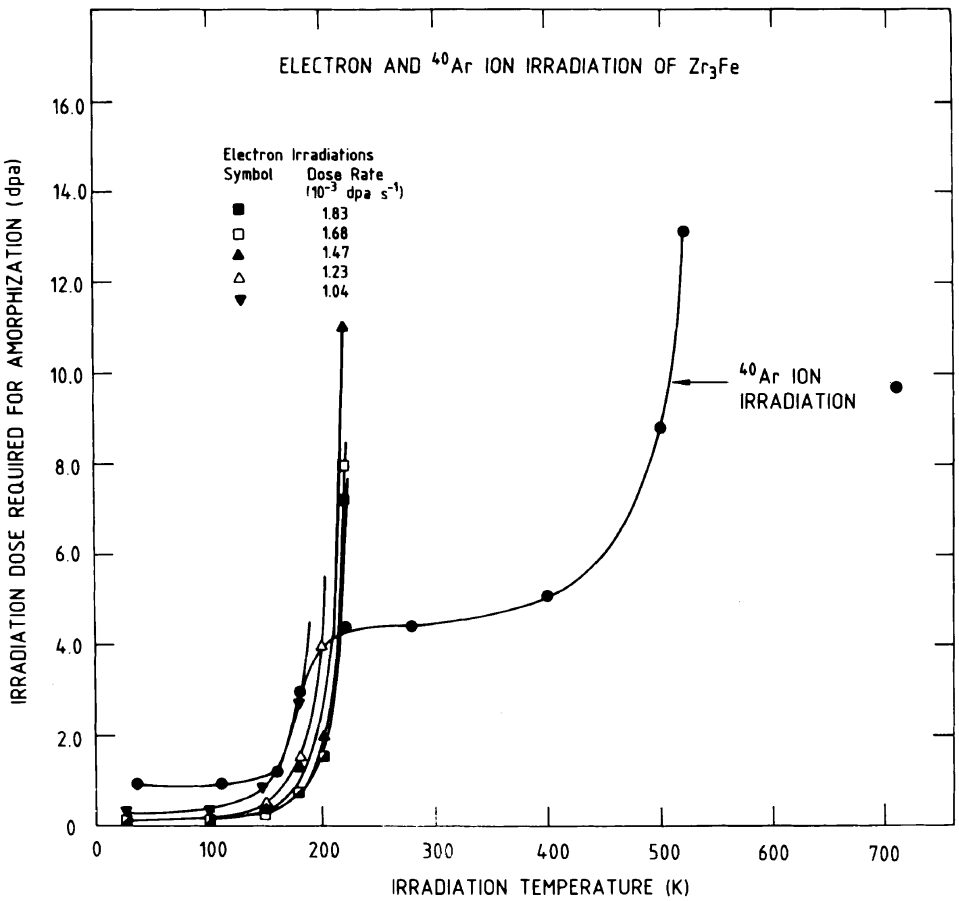


Fig. 11. Dose to amorphization for $Zr_3Fe$ under electron and Ar ion irradiation.

nealing dispersed damage. Thus the annealing mechanisms that are effective at eliminating the dispersed damage caused by electron irradiation are ineffective in eliminating ion damage. At a much higher temperature, the amorphous zones formed by single or multiple cascade impacts become unstable and are recrystallized continuously during irradiation, so that the achievable amorphous volume fraction is very small. It is interesting to note that once a phase is made completely amorphous at low temperature, heating it above the critical temperature for amorphization does not necessarily cause crystallization to occur. To cause recrystallization, it is often necessary to heat the material to 200–300 K above $T_c$ (less for $Zr_3Fe$). This is likely the difference between homogeneous nucleation of the crystal from the amorphous phase and the advancement of a crystalline front into the amorphous region. The latter process likely requires a lower activation energy than the former.

We also note that amorphization under ion irradiation is affected by dose rate [21,49]. For a given temperature, it has been observed that the critical dose for amorphization of $Zr_3Fe$ decreases as the dose rate increases. No detailed studies have yet been performed on the influence of dose rate on the critical temperature for ion induced amorphization of $Zr_3Fe$, but it is likely that an effect similar to that observed under electron irradiation would exist. On the basis of TEM observations of amorphous regions produced by individual collision cascades in $Zr_2Fe$, $Zr_3Fe$ and $ZrFe_2$ during heavy ion bombardments, Howe et al. [21,49,50] propose that during ion bombardment amorphization can occur directly in the heavily damaged regions of the cascade or by the gradual accumulation of defects in the areas of cascade overlap. This is in agreement with the mechanisms proposed by Howe et al. [51–53] and Rualt [54,55] for the amorphization of Si and Ge during heavy ion bombardment.

## 5. Conclusions

1. A systematic study has been conducted of the amorphization behavior of $Zr_3Fe$ under electron irradiation. By performing the irradiation in situ, it was possible to obtain detailed information on the kinetics of the process.

2. The critical dose-to-amorphization of $Zr_3Fe$ increases exponentially with temperature, so that above a critical temperature it is not possible to amorphize the material with electron irradiation. The critical temperature for amorphization of $Zr_3Fe$ under electron irradiation is about 220 K, which corresponds well to an annealing stage observed during amorphization by Ar ion irradiation.

3. The critical temperature for amorphization increases with increasing dose rate. A variation of about 10 K is achieved by doubling the dose rate.

4. The dose-to-amorphization increases with decreasing electron energy, in a manner consistent with displacements being possible in both sublattices at high energy, in one sublattice at intermediate energies, and not possible at low energies.

5. The dose-to-amorphization vs. electron energy curve was used to determine the displacement energies in the individual sublattices in the $Zr_3Fe$ intermetallic compound; they were $E_d^{Zr} = 26$ eV and $E_d^{Fe} = 18$ eV.

6. At low electron energies (<400 keV) the amorphization rate depends on the crystalline orientation relative to the electron beam.

7. These results can be well understood using a chemical rate theory model that predicts the dose-to-amorphization by the slow accumulation of point defects, under a recombination-dominated regime dominated by the surface sink. Amorphization occurs when the free energy of the defected crystal exceeds that of the amorphous phase.

## Acknowledgements

The authors would like to thank D. Phillips of Chalk River Laboratories for his technical assistance, as well as E. Ryan and S. Ockers of Argonne National Laboratories, for their technical assistance during the experiments. This research program was partly funded through a CANDU Owners Group (COG) contract in working party 32 and by the National Science Foundation under grant INT-9503934.

## References

[1] G. Thomas, H. Mori, H. Fujita, R. Sinclair, Scr. Metall. 16 (1982) 589.
[2] A. Mogro-Campero, E.L. Hall, J.L. Walter, A.J. Ratkowski, in: S.T. Picraux, W.J. Choike (Eds.), Metastable Phase Formation by Ion Implantation, Elsevier Science, Lausanne, 1982, p. 203.
[3] A.T. Motta, J. Nucl. Mater. 244 (1997) 227.
[4] P.R. Okamoto, M. Meshii, in: H. Wiedersich, M. Meshii (Eds.), Science of Advanced Materials, American Society of Metals, Cleveland, OH, 1992, p. 33.
[5] R.W. Cahn, W.L. Johnson, J. Mater. Res. 1 (1986) 724.
[6] M. Nastasi, J.W. Mayer, Mater. Sci. Rep. 6 (1991) 3.
[7] N.Q. Lam, P.R. Okamoto, Mater. Res. Soc. Bull. (1994) 41.
[8] D.F. Pedraza, Metall. Trans. 21A (1990) 1809.
[9] A.T. Motta, C. Lemaignan, in: A.R. Yavari (Ed.), Ordering and Disordering in Alloys, Elsevier, 1992, p. 255.
[10] C. Jaouen, Solid State Phenomena 23&24 (1992) 123.
[11] P.R. Okamoto, N.Q. Lam, L.E. Rehn, in: H. Ehrenreich, F. Spapen (Eds.), Solid State Physics, 1998.
[12] L.M. Howe, in: J.H. Westbrook, R.L. Fleischer (Eds.), Intermetallic Compounds, vol. I: Principles, Wiley, 1994, p. 791.

[13] A.T. Motta, D.R. Olander, Acta Metall. Mater. 38 (1990) 2175.
[14] D.E. Luzzi, M. Meshii, Res. Mechan. 21 (1987) 207.
[15] J. Brimhall, H.E. Kissinger, L.A. Charlot, Radiat. Eff. 77 (1983) 273.
[16] H. Mori, M. Fujita, Tendo, M. Fujita, Scr. Metall. 18 (1984) 783.
[17] A.T. Motta, L.M. Howe, P.R. Okamoto, J. Nucl. Mater. 205 (1993) 258.
[18] J. Koike, Metall. Trans. 21A (1990) 1799.
[19] J. Koike, P.R. Okamoto, L.E. Rehn, J. Mater. Res. 4 (1989) 1143.
[20] N.Q. Lam, P.R. Okamoto, M. Sabochik, R. Devanathan, J. Alloys Compounds 194 (1993) 429.
[21] L.M. Howe, D. Phillips, H.H. Plattner, J.D. Bonnett, Nucl. Instrum. Meth. 102 (1995) 77.
[22] L.M. Howe, D. Phillips, A.T. Motta, P.R. Okamoto, Surf. Coat. Technol. 66 (1994) 411.
[23] A.T. Motta, L.M. Howe, P.R. Okamoto, in: I.M. Robertson, L.E. Rehn, S.J. Zinkle, W.J. Phythian (Eds.), Microstructure of Irradiated Materials, vol. 373, Materials Research Society Symposium Proceedings, Materials Research Society, 1995, p. 183.
[24] A.T. Motta, J.A. Faldowski, L.M. Howe, P.R. Okamoto, in: E.R. Bradley, G.P. Sabol (Eds.), 11th Int. Symposium on Zr in the Nuclear Industry, Garmisch–Partenkirchen, ASTM STP 1295, 1996, p. 557.
[25] J.A. Faldowski, A.T. Motta, L.M. Howe, P.R. Okamoto, Thermodynamics and Kinetics of Phase Transformations, Boston, MA, MRS Symposium Proceedings 398, 1996, p. 183.
[26] F. Aubertin, U. Gonser, S.J. Campbell, H.-G. Wager, Z. Metallkd. 76 (1985) 237.
[27] C. Hausleitner, J. Hafner, J. Non-Cryst. Solids 144 (1992) 175.
[28] A.T. Motta, D.R. Olander, A.J. Machiels, 14th International Symposium on Effects of Radiation on Materials, Andover, Ma, American Society for Testing Materials STP 1046, 1989, p. 457.
[29] R. Devanathan, N.Q. Lam, P.R. Okamoto, M. Meshii, Phys. Rev. B 48 (1993) 42.
[30] P. Bellon, G. Martin, Mater. Res. Soc. Bull. 11 (1991) 33.
[31] J.A. Faldowski, A.T. Motta, L.M. Howe, P.R. Okamoto, J. Appl. Phys. 80 (2) (1996) 729.
[32] L.M. Howe, D. Phillips, H. Zou, J. Forster, R. Siegele, J.A. Davies, A.T. Motta, J.A. Faldowski, P.R. Okamoto, Nucl. Instrum. Meth. 118 (1996) 663.
[33] H. Mori, M. Nakamina, H. Fujita, 11th International Congress on Electron Microscopy, Kyoto, 1986, p. 1101.
[34] E.P. Simonen, Nucl. Instrum. Meth. 16 (1986) 198.
[35] P. Gordon, Principles of Phase Diagrams, Ch. 4, McGraw-Hill, New York, 1968.
[36] R. Zee, P. Wilkes, Philos. Mag. A 42 (1980) 463.
[37] S. Banerjee, K. Urban, Phy. Status Solidii (a) 81 (1984) 145.
[38] D.F. Pedraza, L.K. Mansur, Nucl. Instrum. Meth. B 16 (1986) 203.
[39] J.R. Shoemaker, R.T. Lutton, D. Wesley, W.R. Wharton, M.L. Oehrli, I.S. Herte, M.J. Sabochik, N.Q. Lam, J. Mater. Res. 6 (1991) 473.
[40] F. Maury, P. Vajda, A. Lucasson, P. Lucasson, Radiat. Eff. 10 (1971) 239.
[41] E.A. Kenik, T.E. Mitchell, Philos. Mag. 32 (1975) 815.
[42] P.G. Regnier, N.Q. Lam, J. Nucl. Mater. 133 (1985) 423.
[43] P.G. Regnier, N.Q. Lam, K.H. Westmacott, J. Nucl. Mater. 115 (1983) 186.
[44] O.S. Oen, Oak Ridge National Laboratory Report no. 4897, 1973.
[45] A. Alamo, C.H. deNovion, G. Desarmot, Radiat. Eff. 88 (1986) 69.
[46] F. Rullier-Albenque, J.P. Senateur, Radiat. Eff. 88 (1986) 17.
[47] A. Caro, M. Victoria, R.S. Averback, J. Mater. Res. 5 (1990) 1409.
[48] H. Zhu, N.Q. Lam, R. Devanathan, M. Sabochik, in: G.S. Was, L. Rehn, D.M. Follstadt (Eds.), Phase Formation and Modification by Beam–Solid Interactions, Mater. Res. Soc. Symp. Proc. 235 (1992) 533.
[49] L.M. Howe, M.H. Rainvile, D. Phillips, Materials Research Society Fall Meeting, Boston, MRS Symp. Proc. 235 (1992) 461.
[50] L.M. Howe, M. Rainville, D. Phillips, H. Plattner, J.D. Bonnett, Nucl. Instrum. Meth. B 80&81 (1993) 73.
[51] L.M. Howe, M. Rainville, Prac. Mic. Soc. Canada 10 (1983) 64.
[52] L.M. Howe, M. Rainville, Nucl. Instrum. Meth. 19&20 (1987) 61.
[53] L.M. Howe, M. Rainville, in: U. Gibson, A.E. White, P.P. Pronko (Eds.), Materials Modification and Growth Using Ion Beams, Mater. Res. Soc. Symp. Proc. 93 (1987) 79.
[54] M.O. Rualt, J. Chaumont, H. Bernas, Nucl. Instrum. Meth. 209&210 (1983) 351.
[55] M.O. Rualt, J. Chaumont, J.M. Pennisson, A. Bourret, Philos. Mag. A 50 (1984) 667.